THE JOURNAL OF PHYSICAL CHEMISTRY C
Article
Cite This: J. Phys. Chem. C 2018, 122, 27241−27249
pubs.acs.org/JPCC

Extrinsic Defects in Crystalline MoO_3: Solubility and Effect on the Electronic Structure

D. S. Lambert,[†] A. Lennon,[†] and P. A. Burr*[,‡]

[†]School of Photovoltaics and Renewable Energy Engineering and [‡]School of Mechanical and Manufacturing Engineering, UNSW Sydney, Kensington, NSW 2052, Australia

ABSTRACT: The effect of six potential contaminants (Cu, In, Ga, Se, Sn, and Zn) and five potential dopants (Ti, Mn, Sc, V, and Y) on the electronic and optical properties of molybdenum oxide (MoO_3) contact layers for solar cells was investigated using point defect analysis based on density functional theory simulations. Of the contaminants investigated, Sn, In, and Ga were found to be highly insoluble at all relevant temperatures and pressures and therefore not a concern for solar cell manufacturing. Zn, Cu, and Se exhibit some solubility, with the latter two appearing to introduce detrimental defect states near the valence band. This contamination can be avoided by increasing the O_2 partial pressure during MoO_3 deposition. Of the five potential aliovalent dopants, Sc, Ti, and Y were disregarded because of their limited solubility in MoO_3, whereas V was found to be highly soluble and Mn somewhat soluble. The effect of Mn and V doping was shown to be strongly dependent on the O_2 partial pressure during deposition, with a high pO_2 favoring the formation of substitutional defects (potentially beneficial in the case of Mn doping because of the addition of defect states near the conduction band), whereas low pO_2 favoring interstitial defects.

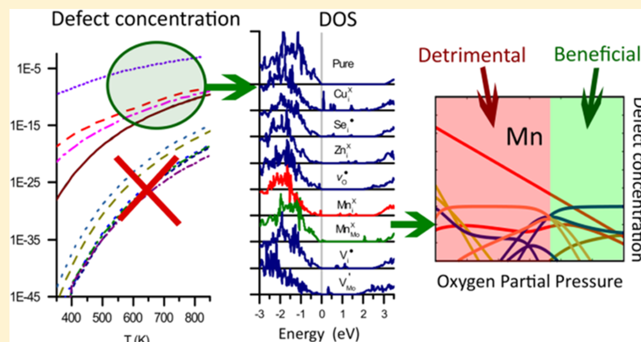

1. INTRODUCTION

Molybdenum oxide (MoO_3) is a material of great interest for a number of applications, including electrochromism, catalysis, sensors, capacitors, and thermoelectric devices.[1] It has been found to be an effective hole contact layer for a range of different photovoltaic devices, including Si cells,[2−4] organic cells,[5,6] quantum dot cells[7] (interfacial layer), perovskite cells,[8−10] and cells with kesterite structure absorbers, such as $Cu_2ZnSnSe_4$ (CZTSe) and $CuIn_xGa_{(1-x)}Se_2$ (CIGS).[11−13] Ranjbar et al.[11] reported that the insertion of an interfacial layer of MoO_3 between the absorber and the back contact improved the absolute cell efficiency of CZTSe cells by 1.2% compared to that of a reference cell, by reducing electron−hole recombination and chemical reactions at the interface between the absorber and the back contact. In Si solar cell applications, MoO_3 has been employed as a hole-selective front contact,[2−4] providing the benefit of reduced parasitic absorption compared to that from the routinely used doped amorphous Si contact layer, producing cell efficiencies as high as 22.5%.[3]

Early applications of MoO_3 carrier-selective contact layers for Si solar cells suffered from band misalignments between the contact and absorber, reducing cell efficiency. Geissbühler et al.[3] were able to overcome this by limiting the processing temperature to 130 °C, which ensured an amorphous MoO_3 layer. However, this temperature limit is incompatible with commercial manufacturing processes used to form metal contacts, such as silver screen printing. Consequently, it has been proposed that the use of crystalline[14] or nanocrystalline[15] structures may allow for higher processing temperatures and improved carrier mobilities. Understanding the electronic structure of crystalline MoO_3 is therefore crucial to addressing these issues and improving device performance.

It is known that the electronic structure of MoO_3 is strongly dependent on the defects present in the film.[4] O vacancy concentration in MoO_3 has been shown to affect the work function,[16] band gap,[17] and conductivity[18] of the material. It has also been suggested that O vacancies induce a defect band within the band gap of MoO_3, which is responsible for the hole conduction properties of the material.[19] In a previous study,[20] we used density functional theory (DFT) to show that the large nonstoichiometry range of the material (MoO_{3-x}) is accommodated by charge-neutral O vacancies, which do not require an accompanying charge-compensating defect. We also predicted the degree of substoichiometry as a function of processing temperature and O_2 partial pressure.

Despite the widespread interest in this material, including several DFT studies investigating point defects,[20−24] there has been little examination of extrinsic defects in MoO_3, with the notable exceptions of H[25] and, in our recent report, Si.[20] In that report, we identified that Si contamination above 1 ppm is likely at temperatures greater than 700 K and O_2 partial pressures lower than 10^{-6} atm. Here, we extend the study to extrinsic defects that are relevant to other solar cell designs that use MoO_3 carrier-selective contact layers and for which there

Received: September 21, 2018
Revised: November 7, 2018
Published: November 8, 2018

Downloaded via UNIV OF NEW SOUTH WALES on January 8, 2019 at 02:23:26 (UTC).
See https://pubs.acs.org/sharingguidelines for options on how to legitimately share published articles.

ACS Publications © 2018 American Chemical Society

DOI: 10.1021/acs.jpcc.8b09226
J. Phys. Chem. C 2018, 122, 27241−27249

appears to be limited understanding of how point defects may affect the device performance. These defects may arise from contact with different absorber materials (e.g., Cu, Zn, Sn, Se, In, and Ga from kesterite cells), contact with different interfacial or capping materials (e.g., In and Sn from indium tin oxide or ITO[4]), and/or from contamination during processing (e.g., Cu from wire sawing of Si ingots into wafers[26]). The feasibility of deliberately doping MoO_3 to alter the electronic structure in a way favorable to solar cell performance has similarly not been considered previously. Therefore, we also examined the transition metals Mn, Sc, Ti, V, and Y as potential aliovalent dopants.

2. METHODS

2.1. Defect Concentration Calculations. Equilibrium defect concentrations are calculated from defect formation energies, coupled with the enforcement of electroneutrality. The Arrhenius expression for the concentration of a defect i is

$$c_i(pO_2, T) = m_i \exp\left(\frac{-\Delta E_f^i(pO_2, T)}{kT}\right) \tag{1}$$

where m_i is the multiplicity of the defect, k is the Boltzmann constant, and ΔE_f^i is the defect formation energy, which is a function of temperature and O_2 partial pressure, as well as the Fermi level (see eq 2). For each T and pO_2, eq 1 was iteratively solved to find the self-consistent Fermi level that produces a balance of charged defect concentrations satisfying electroneutrality, as described in our previous paper.[20] This was done with the aid of the defect analysis program of Murphy et al.[27] The resulting defect concentrations are then plotted against temperature and O_2 partial pressure in the form of Brouwer diagrams.

The defect formation energy, E_f, is calculated using

$$E_f(pO_2, T) = E_{\text{defect}} - E_{\text{host}} \pm \sum_j n_j\mu_j(pO_2, T) + q(E_{\text{VBM}} + \mu_e) + E_{\text{chgcor}} \tag{2}$$

where E_{defect} and E_{host} are the energies of the simulated supercell with and without the defect, respectively. The summation term refers to the chemical potentials μ_j of all of the j atoms that are added (negative) or removed (positive) from the cell to form the defect, μ_e is the Fermi level above the valence band maximum (VBM) E_{VBM}, and E_{chgcor} is a correction term to counter the electrostatic interactions across periodic boundary conditions. The latter term is nearly negligible in our calculations, but still included, as we exploited the strong dielectric anisotropy of the material when choosing the supercell shape, as reported in Lambert et al.[20]

To overcome the inherent limitation of semilocal DFT in describing formation energies of O and oxides,[28] the chemical potentials of Mo and O were calculated following the method of Finnis et al.[29] By linking the chemical potential to the Gibbs free energy of formation, the concentration of defects can be predicted as a function of T and pO_2. This method is well-established for intrinsic defects,[27] but the current study requires an extension of the method to account for the chemical potential of extrinsic defects, presented below.

2.2. Chemical Potentials of Extrinsic Species. To determine the formation energy of extrinsic defects in MoO_3, the chemical potentials of those species in the reference oxide must also be determined. A wide variety of methods have been used to determine the reference chemical potential of extrinsic defects.[30−35] Previous studies determined these potentials through direct DFT calculation of the oxide;[20] however, this can cause problems as many of the reference oxides require the addition of $+U$ terms of differing magnitudes to the metal atom for accurate simulations, making it difficult to compare between them. In addition, DFT is known to overestimate the formation energy of many oxides,[36] which could also introduce significant differences in the results.

One solution is to rewrite the chemical potential in terms of the known standard energy of formation of the oxide:[29,36] the free energy of formation for a binary metal oxide M_xO_y under standard conditions is defined as

$$\Delta G_f^{M_xO_y}(pO_2^0, T^0) = \mu_{M_xO_y(s)} - x\mu_{M(s)} - \frac{y}{2}\mu_{O_2(g)}(pO_2^0, T^0) \tag{3}$$

Here, we have implicitly removed the dependence of the solid phases on temperature and partial pressure, as it is negligible compared to that of the gaseous phase. Rearranging eq 3 gives us an expression for the chemical potential of the reference oxide $\mu_{M_xO_y(s)}$

$$\mu_{M_xO_y(s)} = \Delta G_f^{M_xO_y}(pO_2^0, T^0) + x\mu_{M(s)} + \frac{y}{2}\mu_{O_2(g)}(pO_2^0, T^0) \tag{4}$$

By construction, the chemical potential of the constituent species in the oxide must add up to the chemical potential of the oxide

$$\mu_{M_xO_y(s)} = y\mu_{O(M_xO_y)} + x\mu_{M(M_xO_y)} \tag{5}$$

and if we assume that the oxide is in thermodynamic equilibrium with the surrounding air, then

$$\mu_{O(M_xO_y)}(pO_2, T) = \frac{1}{2}\mu_{O_2(g)}(pO_2, T) \tag{6}$$

which provides us with an equation for $\mu_{M(M_xO_y)}$

$$\mu_{M(M_xO_y)}(pO_2, T) = \frac{1}{x}\left(\mu_{M_xO_y(s)} - \frac{y}{2}\mu_{O_2(g)}(pO_2, T)\right) \tag{7}$$

Combining eqs 4 and 7, we find an expression for the chemical potential of the metal ion in the reference oxide

$$\mu_{M(M_xO_y)}(pO_2, T) = \frac{1}{x}\left(\Delta G_f^{M_xO_y}(pO_2^0, T^0) + x\mu_{M(s)} + \frac{y}{2}\mu_{O_2(g)}(pO_2^0, T^0) - \frac{y}{2}\mu_{O_2(g)}(pO_2, T)\right) \tag{8}$$

where the dependence on T and pO_2 of $\mu_{O_2(g)}$ is captured with a rigid-dumbbell ideal gas model (as is commonly done for intrinsic defects[27,37,38]), $\Delta G_f^{M_xO_y}(pO_2^0, T^0)$ is taken from standard chemical tables,[39] and $\mu_{M(s)}$ is obtained from a DFT simulation of the metal crystal. This method ensures that the chemical potentials of both intrinsic and extrinsic defects are internally consistent and largely insensitive to the computational methodology.

2.3. Computational Methods. DFT calculations were performed using the Vienna ab initio simulation package.[40]

DOI: 10.1021/acs.jpcc.8b09226
J. Phys. Chem. C 2018, 122, 27241−27249

Table 1. Number of Valence Electrons Used for Modeling the 12 Elements

element	Mo	O	Mn	Sc	Ti	V	Y	Cu	Zn	Sn	Se	In
valence electrons	14	6	15	11	12	13	11	17	12	14	6	13

Defect relaxations were performed at constant volume using the Perdew−Burke−Ernzerhof (PBE) exchange−correlation functional[41] and with the rotationally invariant on-site Coulomb correction[42] (+U) of 6.3 eV applied to the Mo d orbital, consistent with previous studies.[43−46] van der Waals forces were accounted for with the use of the D3 method by Grimme et al.[47] The electronic energy convergence criterion for SCF steps was 2×10^{-7} eV. All defect calculations were relaxed at constant volume in a prerelaxed 192-atom supercell of MoO_3 until the energy difference between two consecutive steps was less than 10^{-5} eV. A supercell consisting of $2 \times 2 \times 3$ MoO_3 unit cells (192 atoms) was chosen as this size exhibits near-zero Madelung potential, thereby almost eliminating the effect of electrostatic self-interactions across periodic boundaries. Details of the convergence of the finite size effect can be found in our previous report.[20] A $3 \times 1 \times 2$ k-point mesh was used to sample the supercells with a Gaussian smearing of 0.1 eV. Projector-augmented wave pseudopotentials were used with a 500 eV energy cutoff, consistent with previous work on transition metal oxides.[23,43,48] The number of valence electrons used for each atom type is listed in Table 1.

Although the PBE functional is known to provide qualitatively accurate forces and energies for transition metal oxides, it widely underestimates the band gap of MoO_3.[48] In contrast, the hybrid functional of Heyd−Scuseria−Ernzerhof[49] (HSE06) has been shown to produce accurate electronic band gaps for MoO_3.[46,48] Thus, to gain quantitative information on how extrinsic defects affect the electronic structure of MoO_3, the most relevant defects were simulated again using the hybrid HSE06 functional, keeping all simulation parameters the same, apart from the use of the tetrahedron smearing method with Blöchl corrections.[50] Due to the prohibitive computational cost of performing geometry relaxations with the HSE06 functional in these large cells, these calculations were restricted to single-point calculations of the prerelaxed PBE configuration, scaled to the size of the HSE06 structure using the strains between the pristine PBE cells and the pristine HSE06 MoO_3 supercells. In the case of V_{Mo}', applying this scaling method to a single-point HSE06 calculation reduced the external cell pressure from 30.36 kB (before scaling) to 9.19 kB (after scaling), which is in reasonable agreement with the 5.04 kB defect relaxation pressure of the relaxed PBE cell. Although this method does not ensure that the defect and its neighboring atoms will be fully relaxed, it is a suitable compromise that enables a hybrid functional investigation of a 192-atom cell, which would otherwise be impracticable.

3. RESULTS AND DISCUSSION

3.1. Defect Formation Energies. To the best of our knowledge, no experimental information is available on the stability of interstitial sites in MoO_3. However, these were not discounted a priori; instead, we explicitly calculate the energy of both interstitial and substitutional defects, under all plausible charge states, for all defects. When the formation energy of interstitial defects is significantly higher than that of the substitutional counterpart, their relative contributions become negligible by construction.

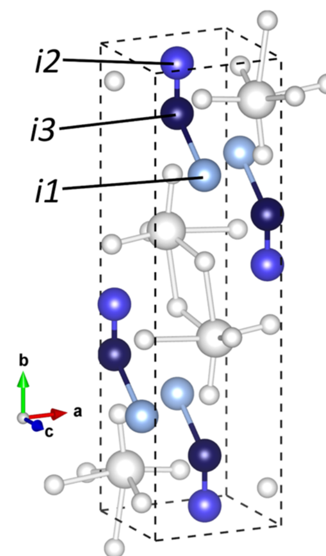

Figure 1. Stable interstitial sites in the unit cell of MoO_3, labeled as i1, i2, and i3.

In the DFT literature, three stable sites have been reported for Mo[20] and Mg[51] interstitials in MoO_3 (see Figure 1). Two of these, the i2 and i3 sites, have also been reported to be stable for Na and K ions in a DFT study by Tahini et al.[23] All three sites were simulated for charge-neutral interstitials of each species. To reduce the otherwise vast number of simulations required, only the most stable interstitial site for each species was then simulated under all plausible charged states, under the assumption that the relative occupancy of the sites would not change significantly for differently charged defects. Most species preferentially occupy the i1 interstitial site inside the van der Waals planes, with the exception of In, Ga, and Mn, which favor the i2 site. No species preferentially occupied the i3 site, and in the cases of Mn, the i3 site was unstable and collapsed into the i2 site.

Figures 2a−c and 2d−f shows the formation energies at standard conditions (T = 298.15 K, pO_2 = 0.2 atm) of substitutional (for Mo) and interstitial elemental defects, respectively, as a function of Fermi level. These are split into three groups: one group of dopants and two groups of contaminants (for ease of viewing). In each graph, only the lowest formation energy defect for each species at a particular Fermi energy is shown. A change in dominant charge state appears as a change of slope of the rectilinear plot.

For all species, substitutional defects are favored at high Fermi levels, whereas interstitial defects are favored at low Fermi levels. This is consistent with the lower oxidation state of all species considered here compared to the 6+ oxidation state of Mo in MoO_3. Notably, V exhibits a negative formation energy (i.e., exothermic solution) when the Fermi level is very close to the valence band maximum (VBM) or the conduction band maximum (CBM). This is unusual and indicative of high solubility at both high and low free electron energies. All other species exhibit positive formation energies at all Fermi levels.

3.2. Predicted Defect Concentrations. The total concentrations of all interstitial and substitutional defects of

DOI: 10.1021/acs.jpcc.8b09226
J. Phys. Chem. C 2018, 122, 27241−27249

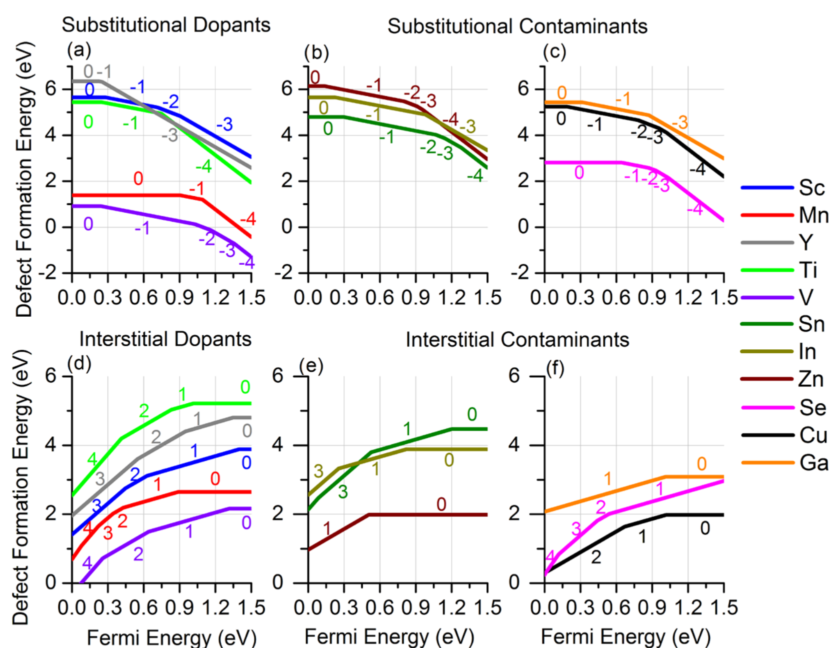

Figure 2. Defect formation energies as a function of Fermi level at standard conditions for substitutional (a, b, c) and interstitial (d, e, f) extrinsic elemental defects. The 11 defects are split into two groups, dopants (left) and contaminants (middle and right), for ease of viewing. In each graph, only the lowest energy defect for each species at a given Fermi level is shown.

each element under different conditions of pO_2 and T were calculated as described in Section 2.1, with the resulting concentrations shown in Figure 3. There is a clear trend for defect concentrations to increase under conditions of high temperature and/or low O_2 partial pressure.

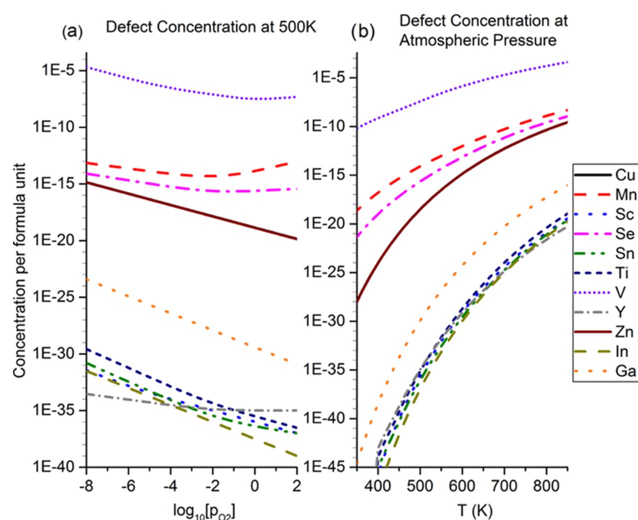

Figure 3. Equilibrium solubility limit for all 11 elemental species at (a) temperature of 500 K and varied O_2 partial pressure conditions and (b) atmospheric pressure and varied temperature. The curves for Zn and Cu are overlapping.

Many of the species investigated were clearly not soluble in MoO_3 under any conditions considered. For example, even at MoO_3's melting temperature of 1068 K under atmospheric conditions, the predicted concentration of Sn defects in the crystal was only 0.002 parts per trillion (ppt). This is consistent with a study by Gaigneaux et al. that attempted to create a ternary Sn−Mo−O solid solution at 823 K, resulting instead in a two-phase mixture of Mo-doped SnO_2 and pure MoO_3.[5252]

Of the 11 species investigated, five display moderate solubility in MoO_3, with concentrations above 1 ppt at atmospheric pressure and 800 K. These comprise V, Mn, Zn, Cu (nearly identical concentrations with Zn), and Se. Of these candidates, V appears to be most easily accommodated within the MoO_3 crystal structure, reaching a predicted concentration of 1 ppm at ∼590 K and atmospheric pressure. It should be noted that these solubility predictions are based on the thermodynamic considerations only and that the solubility of some of these defects may be limited by diffusion kinetics. Additionally, entropic effects in the solid phases (e.g., vibrational and configurational entropies) were not included in the analysis.

3.3. Contamination from Specific Photovoltaic Materials. The defect concentrations were grouped by the potential sources of contamination: the PV substrates CIGS, CZTSe, and ITO. For each material, we considered all of the possible defects that could occur and produced Brouwer diagrams for a typical processing temperature of 700 K (see Figure 4).

Irrespective of the substrate material, the dominant defects are intrinsic O vacancies (charge-neutral) and, at sufficiently low pO_2, small amounts of Mo interstitials (also charge-neutral), consistent with intrinsic Brower diagrams of MoO_3.[20] Contact with ITO is not predicted to cause dissolution of In or Sn in MoO_3. For CZTSe and CIGS substrates, some contamination is predicted to occur under low pO_2 conditions. For both of these materials, the dominant extrinsic defects are the charge-neutral Se interstitial ($Se_i^{\times}$ using the Kröger−Vink notation[53]) for $pO_2 < 10^{-8}$ atm, $Cu_i^{\times}$ for $pO_2 = 10^{-6}-10^{-8}$ atm, and $Se_{Mo}^{''''}$ (i.e., charge −4 state) for $pO_2 > 10^{-6}$ atm. For CZTSe, Cu contamination is accompanied by Zn (as $Zn_i^{\times}$), in equal proportions.

3.4. Accommodation of Soluble Species. To examine how the most soluble species are accommodated within MoO_3, a fixed total defect concentration of 1 ppm was enforced by shifting the chemical potential of the reference oxide for each

DOI: 10.1021/acs.jpcc.8b09226
J. Phys. Chem. C 2018, 122, 27241−27249

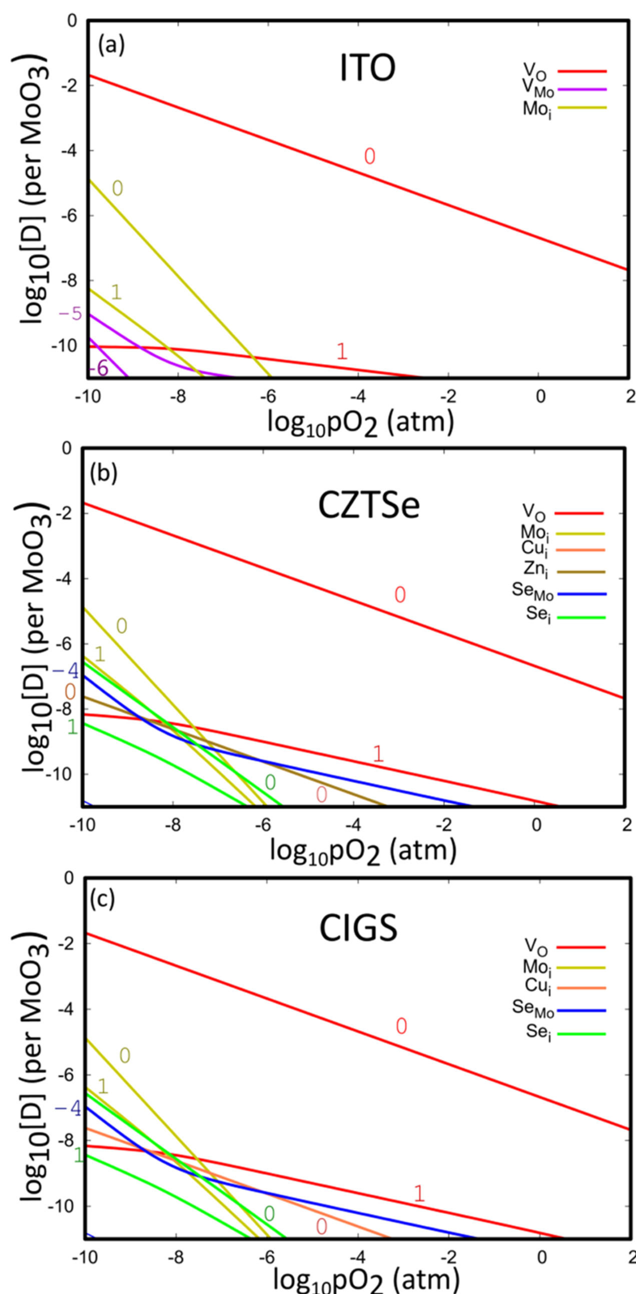

Figure 4. Brouwer diagrams depicting the predicted concentration of defects in MoO_3 at 700 K when in thermodynamic equilibrium with (a) ITO, (b) CZTSe, and (c) CIGS. In (b), the Cu and Zn curves are overlapping.

species while keeping the relative defect energies constant. The resulting Brower diagrams at 700 K are shown in Figure 5. Cu and Zn are accommodated in MoO_3 as charge-neutral interstitials at all pO_2 levels, and therefore, their behavior in the material is independent of the processing conditions. On the other hand, Mn and V exhibit a switch of dominant defect from interstitial defects under low pO_2 conditions to substitutional defects under higher pO_2 conditions. For V, this switch in behavior is coupled with a change in dominant charge state: above 10^{-4} atm, the dominant defect is negatively charged (V_{Mo}'), and below that, it is positively charged ($V_i^{\bullet}$).

Notably, doping MoO_3 with Mn and V leads to a significant increase in 1+ ionic and electronic intrinsic defects (O vacancies and holes) as a charge-compensating mechanism caused by the presence of negatively charged substitutional defects. This suggests the possibility of using Mn and V dopants to increase free hole concentrations in MoO_3 layers, thereby improving the conductivity of the layer. Se is always accommodated as an interstitial defect, but the preferred charge state switches from charge-neutral ($Se_i^{\times}$) to charge +1 ($Se_i^{\bullet}$) as pO_2 increases. However, here, the charge-compensating defects are not intrinsic vacancies and holes but negatively charged substitutions of Se for Mo (Se_{Mo}'''', Se_{Mo}''', Se_{Mo}'', and Se_{Mo}').

3.5. Effect of Extrinsic Defects on Electronic Structure. For the five most soluble species in MoO_3, we calculated the electronic density of states (DOS) of the dominant defects. These calculations were performed using the hybrid HSE06 functional, which has a band gap very close to the experimental band gap of the material,[48] from relaxed PBE structures, scaled with the approach described in Section 2.3. The resulting DOS graphs are shown in Figure 6.

These results can be used to predict the effect of extrinsic defects in MoO_3 on solar cell performance. Defects that significantly reduce the band gap may increase parasitic absorption of light if the MoO_3 contact layer is being used on the sun-receiving surface of the solar cell. Thus, defects such as V_{Mo}' and $Cu_i^{\times}$ are possibly detrimental to the performance of the solar cell if present in sufficiently high concentrations.

Although the effect of defect states within the MoO_3 band gap on device performance is generally poorly understood, it is believed that the hole selectivity of MoO_3 is due to defect bands near the CBM.[4,54] This likely means that defects that induce electronic states in the band gap nearer to the CBM, such as in $Mn_{Mo}^{\times}$ and $Zn_i^{\times}$ (but not $Mn_i^{\times}$), are of less concern or possibly even beneficial to device performance, whereas states closer to the VBM as produced by V_{Mo}', $Cu_i^{\times}$, $Mn_i^{\times}$, and $Se_i^{\bullet}$ will likely be detrimental because of an enhancement of carrier recombination.

The results of Figure 6 can be combined with those of Figure 5 to determine the most favorable preparation conditions for each species. An exemplar case is that of Mn, which displays an ambivalent nature. If a Mn-doped MoO_3 layer is deposited under high pO_2 conditions, the dopant will be accommodated via $Mn_{Mo}^{\times}$ defects, which are not detrimental and possibly even beneficial because of the increase in free hole concentration. However, if the solar cell is processed under low pO_2 conditions, the dopant is expected to form $Mn_i^{\times}$ defects, which introduces low gap states, causing increased parasitic light absorption and charge carrier recombination.

Similarly, when doping MoO_3 with V, it can be seen that V_{Mo}' greatly reduces the band gap of MoO_3 and creates defect states near the VBM. This can be countered by processing at $pO_2 < 10^{-8}$ atm, thereby limiting the concentration of V_{Mo}' in favor of $V_i^{\bullet}$, which is likely to be less detrimental to the device. On the other hand, processing at high pO_2 leads to the formation of free holes, which would be expected to lead to increase the electronic conductivity of the MoO_3 layer. Doping with Mn and V, irrespective of the processing pO_2 condition, is also expected to increase the formation of singularly charged O vacancies as charge compensation mechanisms. This defect reduces the band gap by around 1 eV, but it does not result in any detrimental deep defect states.

DOI: 10.1021/acs.jpcc.8b09226
J. Phys. Chem. C 2018, 122, 27241−27249

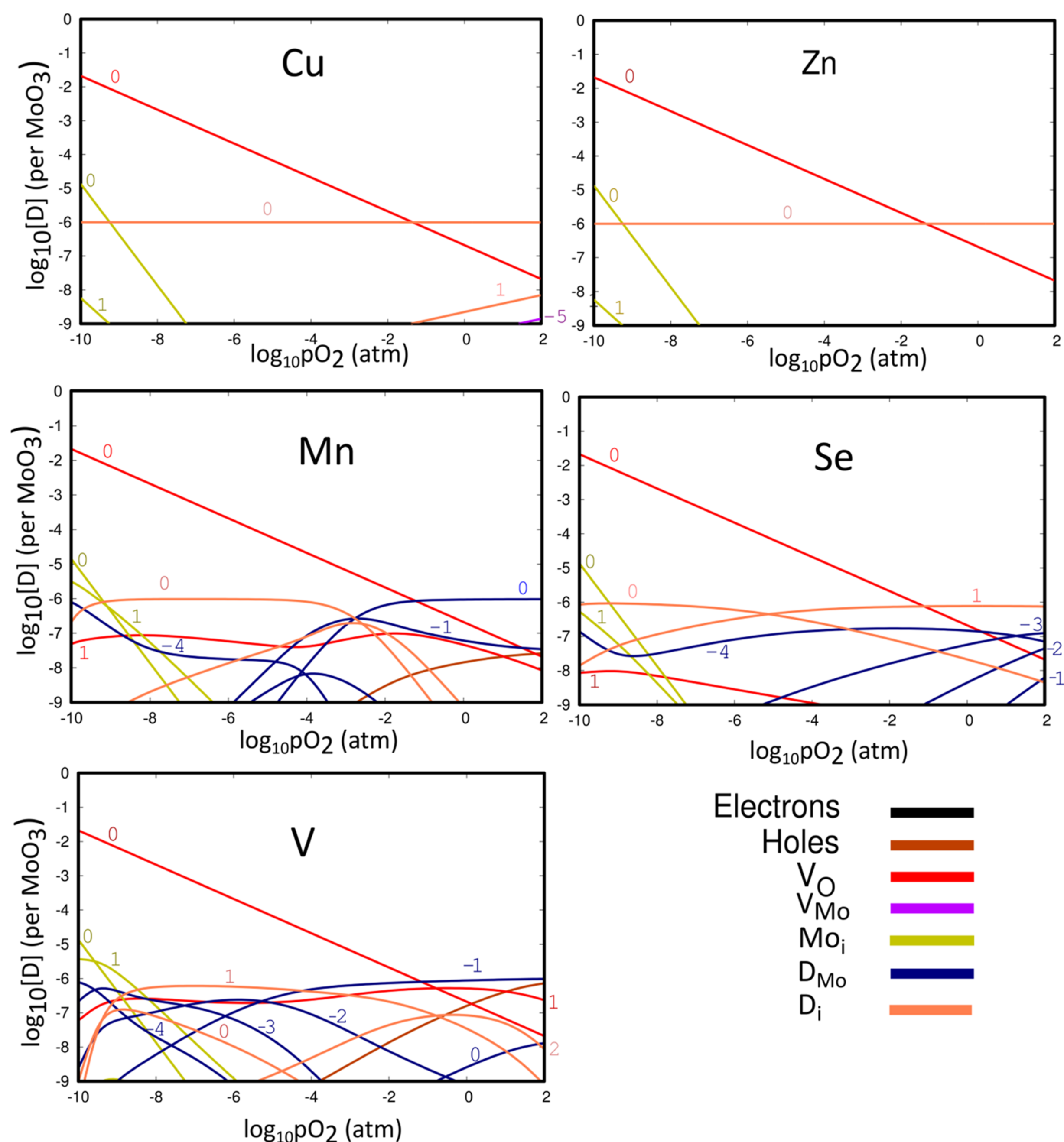

Figure 5. Brouwer diagrams at 700 K showing the most favorable way to accommodate 1 ppm of extrinsic species Cu, Zn, Mn, Se, and V under different pO_2 conditions. D_{Mo} and D_i refer to the substitutional and interstitial defects of each species, respectively.

4. CONCLUSIONS

The solubility of extrinsic elemental species in MoO_3 was investigated using DFT simulations. For those species exhibiting solubility under practical conditions, their effect on the electronic properties of crystalline MoO_3 was evaluated to establish their potential use as dopants or their role as detrimental contaminants. Eleven elements were investigated and selected because of their presence in the range of photovoltaic materials where MoO_3 is being considered as a possible hole-selective contact layer (In, Sn, Cu, Zn, Se, and Ga) or because of being potential aliovalent dopants (V, Mn, Sc, Ti, and Y). A robust treatment of chemical potential was introduced to overcome limitations of DFT modeling of oxides. By relating the chemical potential of all species to the experimental standard energy of formation of the parent oxide, this quantity can be decoupled from the choice of computational methodology to enable the prediction of intrinsic and extrinsic defect concentrations as a function of temperature and O_2 partial pressure.

The defect species found in photovoltaic materials ITO, CZTSe, and CIGS were considered as potential contaminants. It was found that In and Sn from ITO substrates and Ga from CIGS solar cells are not thermodynamically soluble in MoO_3 even at high temperatures and should therefore not pose a concern to photovoltaic device manufacturers considering employing MoO_3 carrier-selective contact layers. Conversely, Cu, Zn, and Se contamination of up to ppt concentration is thermodynamically favorable in MoO_3. A density-of-states analysis showed that Cu and Se contamination was likely to be

DOI: 10.1021/acs.jpcc.8b09226
J. Phys. Chem. C 2018, 122, 27241−27249

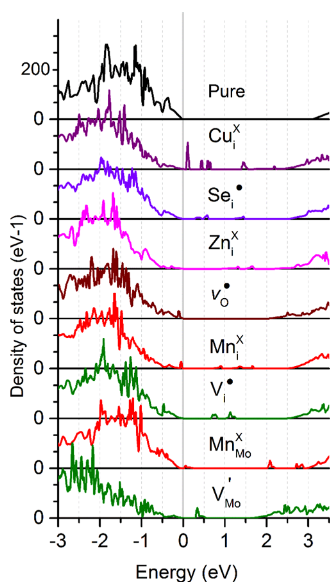

Figure 6. Electronic density of states around the band gap of MoO_3 doped with the most soluble species considered here, as well as the singularly charged O vacancy. The DOS is aligned with the VBM for each defect at 0 eV. All DOS calculations were computed with the HSE06 functional.

more detrimental than that from Zn in that the most dominant defects from those species induce states near the VBM, which would be expected to increase carrier recombination. Our results suggest that the degree of contamination may be reduced by lowering the processing temperature and/or by increasing pO_2 during the deposition of the MoO_3 contact layer on the solar cell absorber material.

Of the potential dopants considered in this study, Sc, Ti, and Y were found to be insoluble, whereas V appeared highly soluble and Mn showed limited solubility. The incorporation of V and Mn dopants in MoO_3 was found to increase the concentration of singularly charged O vacancies and holes, which should act to advantageously increase the conductivity of the MoO_3 contact layer. However, the utility of these dopants is strongly dependent on processing conditions. For example, if Mn is introduced under high pO_2 conditions, it will substitute for Mo as $Mn_{Mo}^{\times}$, which would be of little concern to the device performance, possibly even beneficial because of the formation of band states near the CBM and the increase in free holes. However, if introduced under low pO_2 conditions, it would be accommodated as an interstitial defect $Mn_i^{\times}$ and create lower energy band states that may increase parasitic absorption and carrier recombination. Conversely, for V doping, the low pO_2 dominant $V_i^{\bullet}$ defects were predicted to be less detrimental than the high pO_2 dominant V_{Mo}' defects because of the band gap reduction. This indicates that it should be possible to control the ratio of favorable to unfavorable defect states for MoO_3 doped with Mn or V by processing under high pO_2 or low pO_2 conditions, respectively.

The current findings can be used to guide the use of MoO_3 as a hole-selective contact layer for photovoltaic devices by identifying which types of contamination need to be avoided, identifying possible new dopants that could be used to improve the optical and/or electronic properties of photovoltaic devices, and guiding the preparation conditions that are likely to minimize the presence of detrimental defects. The method used here could be extended to investigate the solubility of extrinsic defects in other carrier-selective transition metal oxide materials, such as TiO_2, V_2O_5, and WO_3.

AUTHOR INFORMATION

Corresponding Author

*E-mail: p.burr@unsw.edu.au. Phone: +61 2 9385 0918.

ORCID

D. S. Lambert: 0000-0002-0288-9128

P. A. Burr: 0000-0003-4796-9110

Notes

The authors declare no competing financial interest.

ACKNOWLEDGMENTS

The authors would like to thank Dr Judy Hart for her advice on hybrid calculations and Dr Samuel Murphy for his assistance with the defect analysis program. This research used the resources and services of the National Computational Infrastructure (NCI), supported by the Australian Government, and the Multi-modal Australian ScienceS Imaging and Visualisation Environment (MASSIVE) (www.massive.org.au). Computational resources were granted through the national merit allocation scheme (NCMAS) and UNSW's "HCP@NCI" trial scheme. Daniel Lambert acknowledges the support of the Australian Government through the award of a Research Training Program (RTP) scholarship. P.A.B. acknowledges the Tyree Foundation and the Australian Nuclear Science and Technology Organisation for financial support. This research was also supported by the Discovery Projects grant DP170103219 from the Australian Research Council.

REFERENCES

(1) de Castro, I. A.; Datta, R. S.; Ou, J. Z.; Castellanos-Gomez, A.; Sriram, S.; Daeneke, T.; Kalantar-zadeh, K. Molybdenum Oxides—from Fundamentals to Functionality. *Advanced Materials* **2017**, *29*, No. 1701619.

(2) Bullock, J.; Cuevas, A.; Allen, T.; Battaglia, C. Molybdenum Oxide MoOx: A Versatile Hole Contact for Silicon Solar Cells. *Appl. Phys. Lett.* **2014**, *105*, No. 232109.

(3) Geissbühler, J.; Werner, J.; de Nicolas, S. M.; Barraud, L.; Hessler-Wyser, A.; Despeisse, M.; Nicolay, S.; Tomasi, A.; Niesen, B.; De Wolf, S.; et al. 22.5% Efficient Silicon Heterojunction Solar Cell with Molybdenum Oxide Hole Collector. *Appl. Phys. Lett.* **2015**, *107*, No. 081601.

(4) Battaglia, C.; Yin, X.; Zheng, M.; Sharp, I. D.; Chen, T.; McDonnell, S.; Azcatl, A.; Carraro, C.; Ma, B.; Maboudian, R.; et al. Hole Selective MoOx Contact for Silicon Solar Cells. *Nano Lett.* **2014**, *14*, 967−971.

(5) Su, Z.; Wang, L.; Li, Y.; Zhang, G.; Zhao, H.; Yang, H.; Ma, Y.; Chu, B.; Li, W. Surface Plasmon Enhanced Organic Solar Cells with a MoO_3 Buffer Layer. *ACS Appl. Mater. Interfaces* **2013**, *5*, 12847−12853.

(6) Fan, X.; Zhang, M.; Wang, X.; Yang, F.; Meng, X. Recent Progress in Organic-Inorganic Hybrid Solar Cells. *J. Mater. Chem. A* **2013**, *1*, 8694−8709.

(7) Brown, P. R.; Lunt, R. R.; Zhao, N.; Osedach, T. P.; Wanger, D. D.; Chang, L.-Y.; Bawendi, M. G.; Bulovic, V. Improved Current Extraction from ZnO/PbS Quantum Dot Heterojunction Photovoltaics Using a MoO3 Interfacial Layer. *Nano Lett.* **2011**, *11*, 2955−2961.

(8) Zhao, Y.; Nardes, A. M.; Zhu, K. Effective Hole Extraction Using MoOx-Al Contact in Perovskite CH3NH3PbI3 Solar Cells. *Appl. Phys. Lett.* **2014**, *104*, No. 213906.

(9) Wu, S.-H.; Lin, M.-Y.; Chang, S.-H.; Tu, W.-C.; Chu, C.-W.; Chang, Y.-C. A Design Based on a Charge-Transfer Bilayer as an

Electron Transport Layer for Improving the Performance and Stability in Planar Perovskite Solar Cells. *J. Phys. Chem. C* **2018**, *122*, 236−244.

(10) Chen, J.; Park, N.-G. Inorganic Hole Transporting Materials for Stable and High Efficiency Perovskite Solar Cells. *J. Phys. Chem. C* **2018**, *122*, 14039−14063.

(11) Ranjbar, S.; Brammertz, G.; Vermang, B.; Hadipour, A.; Cong, S.; Suganuma, K.; Schnabel, T.; Meuris, M.; da Cunha, A. F.; Poortmans, J. Improvement of Kesterite Solar Cell Performance by Solution Synthesized MoO3 Interfacial Layer. *Phys. Status Solidi A* **2017**, *214*, No. 1600534.

(12) Simchi, H.; McCandless, B. E.; Meng, T.; Shafarman, W. N. Structure and Interface Chemistry of MoO3 Back Contacts in Cu(In, Ga)Se2 Thin Film Solar Cells. *J. Appl. Phys.* **2014**, *115*, No. 033514.

(13) Sardashti, K.; Chagarov, E.; Antunez, P. D.; Gershon, T. S.; Ueda, S. T.; Gokmen, T.; Bishop, D.; Haight, R.; Kummel, A. C. Nanoscale Characterization of Back Surfaces and Interfaces in Thin-Film Kesterite Solar Cells. *ACS Appl. Mater. Interfaces* **2017**, *9*, 17024−17033.

(14) Sook Oh, M.; Seob Yang, B.; Ho Lee, J.; Ha Oh, S.; Soo Lee, U.; Jang Kim, Y.; Joon Kim, H.; Soo Huh, M. Improvement of Electrical and Optical Properties of Molybdenum Oxide Thin Films by Ultralow Pressure Sputtering Method. *J. Vac. Sci. Technol., A* **2012**, *30*, No. 031501.

(15) Cauduro, A. L.; Dos Reis, R.; Chen, G.; Schmid, A. K.; Méthivier, C.; Rubahn, H.-G. n; Bossard-Giannesini, L.; Cruguel, H.; Witkowski, N.; Madsen, M. Crystalline Molybdenum Oxide Thin-Films for Application as Interfacial Layers in Optoelectronic Devices. *ACS Appl. Mater. Interfaces* **2017**, *9*, 7717−7724.

(16) Greiner, M. T.; Chai, L.; Helander, M. G.; Tang, W. M.; Lu, Z. H. Transition Metal Oxide Work Functions: The Influence of Cation Oxidation State and Oxygen Vacancies. *Adv. Funct. Mater.* **2012**, *22*, 4557−4568.

(17) Kanai, K.; Koizumi, K.; Ouchi, S.; Tsukamoto, Y.; Sakanoue, K.; Ouchi, Y.; Seki, K. Electronic Structure of Anode Interface with Molybdenum Oxide Buffer Layer. *Org. Electron.* **2010**, *11*, 188−194.

(18) Hanson, E. D.; Lajaunie, L.; Hao, S.; Myers, B. D.; Shi, F.; Murthy, A. A.; Wolverton, C.; Arenal, R.; Dravid, V. P. Systematic Study of Oxygen Vacancy Tunable Transport Properties of Few-Layer MoO_{3-x} Enabled by Vapor-Based Synthesis. *Adv. Funct. Mater.* **2017**, *27*, No. 1605380.

(19) Battaglia, C.; De Nicolas, S. M.; De Wolf, S.; Yin, X.; Zheng, M.; Ballif, C.; Javey, A. Silicon Heterojunction Solar Cell with Passivated Hole Selective MoOx Contact. *Appl. Phys. Lett.* **2014**, *104*, No. 113902.

(20) Lambert, D. S.; Murphy, S. T.; Lennon, A.; Burr, P. A. Formation of Intrinsic and Silicon Defects in MoO3 under Varied Oxygen Partial Pressure and Temperature Conditions: An Ab Initio DFT Investigation. *RSC Adv.* **2017**, *7*, 53810−53821.

(21) Inzani, K.; Grande, T.; Vullum-Bruer, F.; Selbach, S. M. A Van Der Waals Density Functional Study of MoO3 and Its Oxygen Vacancies. *J. Phys. Chem. C* **2016**, *120*, 8959−8968.

(22) Guo, Y.; Robertson, J. Origin of the High Work Function and High Conductivity of MoO3. *Appl. Phys. Lett.* **2014**, *105*, No. 222110.

(23) Tahini, H. A.; Tan, X.; Lou, S. N.; Scott, J.; Amal, R.; Ng, Y. H.; Smith, S. C. Mobile Polaronic States in α-MoO3: An Ab Initio Investigation of the Role of Oxygen Vacancies and Alkali Ions. *ACS Appl. Mater. Interfaces* **2016**, *8*, 10911−10917.

(24) Agarwal, V.; Metiu, H. Oxygen Vacancy Formation on α-MoO3 Slabs and Ribbons. *J. Phys. Chem. C* **2016**, *120*, 19252−19264.

(25) Sha, X.; Chen, L.; Cooper, A. C.; Pez, G. P.; Cheng, H. Hydrogen Absorption and Diffusion in Bulk α-MoO3. *J. Phys. Chem. C* **2009**, *113*, 11399−11407.

(26) Choi, S.; Jang, B.; Kim, J.; Song, H.; Han, M. Cu-Contamination of Single Crystalline Silicon Wafers with Thickness of 100 Mm During Multi-Wire Sawing Process. *Solar Energy* **2016**, *125*, 198−206.

(27) Murphy, S. T.; Hine, N. D. Point Defects and Non-Stoichiometry in Li2TiO3. *Chem. Mater.* **2014**, *26*, 1629−1638.

(28) Wang, L.; Maxisch, T.; Ceder, G. Oxidation Energies of Transition Metal Oxides within the GGA+ U Framework. *Phys. Rev. B* **2006**, *73*, No. 195107.

(29) Finnis, M.; Lozovoi, A.; Alavi, A. The Oxidation of NiAl: What Can We Learn from Ab Initio Calculations? *Annu. Rev. Mater. Res.* **2005**, *35*, 167−207.

(30) Scanlon, D. O. Defect Engineering of BaSnO3 for High-Performance Transparent Conducting Oxide Applications. *Phys. Rev. B* **2013**, *87*, No. 161201.

(31) Yin, W.-J.; Wei, S.-H.; Al-Jassim, M. M.; Turner, J.; Yan, Y. Doping Properties of Monoclinic BiVO4 Studied by First-Principles Density-Functional Theory. *Phys. Rev. B* **2011**, *83*, No. 155102.

(32) Bell, B. D. C.; Murphy, S. T.; Burr, P. A.; Grimes, R. W.; Wenman, M. R. Accommodation of Tin in Tetragonal ZrO2. *J. Appl. Phys.* **2015**, *117*, No. 084901.

(33) Bell, B.; Murphy, S.; Grimes, R.; Wenman, M. The Effect of Nb on the Corrosion and Hydrogen Pick-up of Zr Alloys. *Acta Mater.* **2017**, *132*, 425−431.

(34) Wang, H.; Chroneos, A.; Londos, C. A.; Sgourou, E. N.; Schwingenschlögl, U. Doping Strategies to Control a-Centres in Silicon: Insights from Hybrid Density Functional Theory. *Phys. Chem. Chem. Phys.* **2014**, *16*, 8487−8492.

(35) Chroneos, A.; Grimes, R. W.; Tsamis, C. Atomic Scale Simulations of Arsenic−Vacancy Complexes in Germanium and Silicon. *Mater. Sci. Semicond. Process.* **2006**, *9*, 536−540.

(36) Jain, A.; Hautier, G.; Ong, S. P.; Moore, C. J.; Fischer, C. C.; Persson, K. A.; Ceder, G. Formation Enthalpies by Mixing GGA and GGA+*U* Calculations. *Phys. Rev. B* **2011**, *84*, No. 045115.

(37) Cooper, M. W. D.; Murphy, S. T.; Andersson, D. A. The Defect Chemistry of UO2±x from Atomistic Simulations. *J. Nucl. Mater.* **2018**, *504*, 251−260.

(38) Hine, N. D. M.; Frensch, K.; Foulkes, W. M. C.; Finnis, M. W. Supercell Size Scaling of Density Functional Theory Formation Energies of Charged Defects. *Phys. Rev. B* **2009**, *79*, No. 024112.

(39) Robie, R. A.; Hemingway, B. S. *Thermodynamic Properties of Minerals and Related Substances at 298.15 K and 1 Bar (10^5 Pascals) Pressure and at Higher Temperatures*; US Government Printing Office, 1995; Vol. *2131*.

(40) Kresse, G.; Furthmüller, J. Efficient Iterative Schemes for Ab Initio Total-Energy Calculations Using a Plane-Wave Basis Set. *Phys. Rev. B* **1996**, *54*, No. 11169.

(41) Perdew, J. P.; Burke, K.; Ernzerhof, M. Generalized Gradient Approximation Made Simple. *Phys. Rev. Lett.* **1996**, *77*, No. 3865.

(42) Dudarev, S.; Botton, G.; Savrasov, S.; Humphreys, C.; Sutton, A. Electron-Energy-Loss Spectra and the Structural Stability of Nickel Oxide: An LSDA+U Study. *Phys. Rev. B* **1998**, *57*, No. 1505.

(43) Lei, Y.-H.; Chen, Z.-X. DFT+U Study of Properties of MoO3 and Hydrogen Adsorption on MoO3 (010). *J. Phys. Chem. C* **2012**, *116*, 25757−25764.

(44) Coquet, R.; Willock, D. J. The (010) Surface of α-MoO3, a DFT+ U Study. *Phys. Chem. Chem. Phys.* **2005**, *7*, 3819−3828.

(45) Scanlon, D. O.; Watson, G. W.; Payne, D.; Atkinson, G.; Egdell, R.; Law, D. Theoretical and Experimental Study of the Electronic Structures of MoO3 and MoO2. *J. Phys. Chem. C* **2010**, *114*, 4636−4645.

(46) Akande, S. O.; Chroneos, A.; Vasilopoulou, M.; Kennou, S.; Schwingenschlögl, U. Vacancy Formation in MoO3: Hybrid Density Functional Theory and Photoemission Experiments. *J. Mater. Chem. C* **2016**, *4*, 9526−9531.

(47) Grimme, S.; Antony, J.; Ehrlich, S.; Krieg, H. A Consistent and Accurate Ab Initio Parametrization of Density Functional Dispersion Correction (DFT-D) for the 94 Elements H-Pu. *J. Chem. Phys.* **2010**, *132*, No. 154104.

(48) Peelaers, H.; Van de Walle, C. G. First-Principles Study of Van Der Waals Interactions in MoS2 and MoO3. *J. Phys.: Condens. Matter* **2014**, *26*, No. 305502.

(49) Heyd, J.; Scuseria, G. E.; Ernzerhof, M. Hybrid Functionals Based on a Screened Coulomb Potential. *J. Chem. Phys.* **2003**, *118*, 8207−8215.

DOI: 10.1021/acs.jpcc.8b09226
J. Phys. Chem. C 2018, 122, 27241−27249

(50) Blöchl, P. E.; Jepsen, O.; Andersen, O. K. Improved Tetrahedron Method for Brillouin-Zone Integrations. *Phys. Rev. B* **1994**, *49*, No. 16223.

(51) Wan, L. F.; Incorvati, J. T.; Poeppelmeier, K. R.; Prendergast, D. Building a Fast Lane for Mg Diffusion in α-MoO3 by Fluorine Doping. *Chem. Mater.* **2016**, *28*, 6900−6908.

(52) Gaigneaux, E. M.; Carrazan, S.; Ruiz, P.; Delmon, B. Role of the Mutual Contamination in the Synergetic Effects between MoO3 and SnO2. *Thermochim. Acta* **2002**, *388*, 27−40.

(53) Kröger, F.; Vink, H. Relations between the Concentrations of Imperfections in Crystalline Solids. *Solid State Phys.* **1956**, *3*, 307−435.

(54) Shi, J.; Shen, L.; Liu, Y.; Yu, J.; Liu, J.; Zhang, L.; Liu, Y.; Bian, J.; Liu, Z.; Meng, F. MoOx Modified ITO/a-Si:H(P) Contact for Silicon Heterojunction Solar Cell Application. *Mater. Res. Bull.* **2018**, *97*, 176−181.

DOI: 10.1021/acs.jpcc.8b09226
J. Phys. Chem. C 2018, 122, 27241−27249